

## Research Article

# Improved Hole Injection in Bulk Heterojunction (BHJ) Hybrid Solar Cells by Applying a Thermally Reduced Graphene Oxide Buffer Layer

Alfian F. Madsuha <sup>1,2</sup>, Chuyen Van Pham <sup>2</sup>, Michael Eck,<sup>2</sup> Martin Neukom,<sup>3</sup>  
and Michael Krueger <sup>4</sup>

<sup>1</sup>Department of Metallurgy and Materials Engineering, Universitas Indonesia, 16424 Depok, Indonesia

<sup>2</sup>Institute of Microsystems Technology (IMTEK), University of Freiburg, George Koehler Allee 103, 79110 Freiburg, Germany

<sup>3</sup>Fluxim AG, Technoparkstrasse 2, 8406 Winterthur, Switzerland

<sup>4</sup>Carl von Ossietzky Universität Oldenburg, Institute of Physics, Carl-von-Ossietzky Str. 9-11, 26129 Oldenburg, Germany

Correspondence should be addressed to Michael Krueger; michael.krueger@uol.de

Received 8 August 2018; Accepted 12 February 2019; Published 27 March 2019

Academic Editor: Ovidiu Ersen

Copyright © 2019 Alfian F. Madsuha et al. This is an open access article distributed under the Creative Commons Attribution License, which permits unrestricted use, distribution, and reproduction in any medium, provided the original work is properly cited.

In this work, the utilization of graphene oxide (GO), reduced graphene oxide (rGO), and carbon nanotube (CNT) thin films as hole transport and electron-blocking layers in polymer/nanocrystal hybrid solar cells is demonstrated. A simple method has been used to modify the anode of hybrid solar cells by depositing these two solution-processable nanocarbon materials between poly(3,4-ethylenedioxythiophene):poly(4-styrenesulfonate) (PEDOT:PSS) and transparent indium tin oxide (ITO) layers. Upon the use of an rGO interlayer, we found a substantial improvement in power conversion efficiency (PCE) from 2.5% to 3.2% due to a decrease in series resistance ( $R_s$ ). This decrease has been obtained by a careful tuning of the reduction degree of rGO, inducing optimization of the energy band alignment at the solar cell anode. In addition, charge extraction by linearly increasing voltage (CELIV) measurements show an increase in light-induced charge extraction of ca. 50%. Finally, the utilization of rGO as replacement for PEDOT:PSS is also presented. The findings reported in this work demonstrate the excellent potential of rGO as an efficient hole transport material in hybrid solar cells.

## 1. Introduction

Bulk heterojunction (BHJ) solar cells based on solution-processed organic-inorganic hybrid materials have several advantages, such as low-cost fabrication, high efficiency, light weight, and flexible large-area devices [1]. BHJ hybrid solar cells are in principle comparable to organic solar cells (OSCs). The main difference is that inorganic semiconductor QDs are used in replacing fullerene derivatives as electron acceptors [2]. Recent improvements in BHJ polymer/QD hybrid solar cells exceed power conversion efficiency of 4.7% [3], approaching that which is offered by its organic fullerene-based counterparts using the same donor polymer at the efficiency range of 5.24%–5.5% [4, 5]. In BHJ solar cell devices, the hole transport layer (HTL) between the

photoactive layer and the electrodes plays a vital role in affecting the efficiency and stability of solar cell devices. Poly(3,4-ethylenedioxythiophene):poly(styrenesulfonate) (PEDOT:PSS) is a standard material in organic electronics and especially in organic photovoltaics. It has been widely used as a HTL and acts simultaneously as an electron-blocking layer. PEDOT:PSS is also used for band energy level alignment by reducing the energy barrier between the ITO and the HOMO of the active layer material [6].

However, a severe problem reported in BHJ hybrid solar cells is the lack of long-term stability, which has been given inadequate attention by the scientific community so far [7, 8]. Therefore, simultaneously achieving high efficiency and long-term stability in BHJ solar cells has become a serious challenge. The ITO/PEDOT:PSS interface is considered

to have chemical instability [9–11]. ITO anode is highly vulnerable to corrosion [12, 13] as undesired nature of hygroscopic PEDOT and acidic PSS inherently corrode ITO anodes over time [9, 14]. This condition leads to the degradation of the device performance and stability and thus may undermine the potential of PEDOT:PSS as a suitable HTL [7, 15, 16].

Several alternative materials such as trifluoropropyltrichlorosilane (TFPS),  $\text{MoO}_3$ , NiO,  $\text{V}_2\text{O}_5$ , and  $\text{WO}_3$  have been exploited as HTLs [17]. Recently, graphene-based materials have been considered a feasible candidate for new HTL material due to their tuneable optical properties, high electrical conductivity, thermal and chemical stability, and solution processability [18]. For example, a 10 nm graphene film obtained from thermally reduced graphite oxide displays a high conductivity of 550 S/cm and an optical transparency of more than 70% between 1000 nm and 3000 nm [19]. Compared to PEDOT:PSS, aside from higher optical transparency, thin films of graphene oxide (GO) HTLs are less corrosive to the ITO electrode. On top of that, the large band gap of GO effectively inhibits carrier recombination at the electrode interface by blocking the electron flow towards the anode [17]. Eda et al. first reported the utilization of GO as a HTL in OSCs [20]. Since then, the incorporation of GO as an HTL system is generally found in OSCs. However, to our knowledge, similar results for BHJ hybrid solar cells have not been reported to date.

The solution-processed GO has emerged as the most promising way to produce large quantities of graphene-type materials [21]. GO can be obtained through the sequence of wet chemical methods, including oxidation of natural graphite to graphite oxide, then followed by the exfoliation to GO. However, this method introduces some oxygen-containing functional groups such as epoxy and hydroxyl to the basal plane of GO [22], which disrupts the  $\text{sp}^2$  conjugation, hence making GO an electric insulator [23, 24]. This limitation causes a higher series resistance ( $R_s$ ) with a concomitant lower fill factor (FF) and ultimately lower photoconversion efficiency (PCE) of the resulting devices [25]. Therefore, the improvement in electrical transport properties can be simply achieved by reducing oxygen functionalities from GO, which simultaneously alters GO work function (WF) [26]. The reduced GO (rGO) can be obtained by thermal annealing or chemical reduction reactions [27–29]. It is well documented that the rGO WF is strongly dependent on the oxygen content [24]. The high residual oxygen content leads to larger WF [30–32], while surface functionalization due to introduction of electron-donating groups (EDG) (e.g., thiol (SH)) in GO decreases the WF [33].

Our work is aimed at providing a suitable solution-processed rGO layer that is compatible with device fabrication techniques of BHJ hybrid solar cells. In the present study, we demonstrate the utilization of rGO thin films in HTL of BHJ hybrid solar cells. Two different schemes were investigated: (I) rGO was incorporated as a buffer layer between ITO and PEDOT:PSS and (II) rGO was used as a direct replacement for PEDOT:PSS. For the buffer layers, three different GO reduction approaches were observed which represent the three different degrees of reductive

environments: weak, medium, and strong. Consequently, it was expected to produce three different WFs which affect the overall performance of photovoltaic devices. The devices employing thermal buffer layers of treated rGO thin films yielded efficiency values that are higher than those of devices using solely PEDOT:PSS as the HTL. In addition, films out of multiwalled carbon nanotubes (MWCNT) were also assigned as the HTL for comparison purposes.

## 2. Materials and Methods

Thiol-functionalized rGO was synthesized by refluxing GO together with phosphorus pentasulfide ( $\text{P}_4\text{S}_{10}$ ) in dimethylformamide (DMF) ( $\geq 99.8\%$ , Carl Roth) at  $120^\circ\text{C}$  under vacuum for 24 hours. The thiolated GO flakes were filtered by a Whatman NL16 polyamide  $0.2\ \mu\text{m}$  membrane. The products were then redispersed in DMF and sonicated to obtain a stable suspension of 1 mg/mL.

Aqueous suspension of MWCNTs was obtained according to the procedure reported in the literature [34]. In brief, pristine MWCNTs (Baytubes, Bayer Material Science) were sonicated for 24 hours at  $70^\circ\text{C}$  in a mixture of concentrated  $\text{HNO}_3$  and  $\text{H}_2\text{SO}_4$  with the volume ratio of 3 : 1. Afterwards, oxidized MWCNTs were intensively washed with water and then centrifuged several times for one hour at 4000 rpm until pH  $\sim 7$  value was reached. The precipitates of MWCNTs were redispersed in DI water and sonicated for 1 h to obtain a homogeneous aqueous suspension at 0.02 mg/mL.

Highly crystalline CdSe QDs with an average diameter of 6 nm were synthesized by a hot injection method, according to the procedure reported by Yuan et al. [35]. CdSe QDs showed a full width at half maximum (FWHM) value of 24.5 nm, a first excitonic absorption peak at about 630 nm, and a PL emission at 645 nm. Postsynthetic treatment was conducted on CdSe QDs using hexanoic acid. The detailed washing procedure has been published elsewhere [36]. Afterward, CdSe QDs were dissolved in chlorobenzene (CB) at a concentration of 20 mg/mL.

The devices were fabricated on a structured ITO substrate ( $\leq 10\ \Omega\text{sq}$ , Präzisions Glas & Optik GmbH), which was pretreated for 15 min with oxygen plasma. HTL was configured in the following fashion: ITO/MWCNT/PEDOT:PSS, ITO/rGO/PEDOT:PSS, ITO/CNT, and ITO/rGO, whereas ITO/PEDOT:PSS served as the reference configuration. For the buffer layer rGO/PEDOT:PSS, three reduction approaches of rGO films were performed, namely, condition (a), condition (b), and condition (c). In condition (a), the rGO film was obtained from the spin coating of GO solution followed by thermal reduction at  $300^\circ\text{C}$  for 1 hour in air. Condition (b) was similar to condition (a), except that the reductive annealing was performed in a nitrogen atmosphere (glove box). As for condition (c), the rGO film was obtained from a chemical reduction by thiol functionalization, followed by thermal annealing at  $300^\circ\text{C}$  for 1 hour in air, as reported in the literature [34]. These nanocarbon-based materials were spin-coated at 1100 rpm for 30 s, followed by an additional 1 min drying step at 3000 rpm. PEDOT:PSS (Baytron AI4083 HC Starck) was dissolved in isopropanol and spin-coated at 3000 rpm for 30 s. A photoactive layer of CdSe

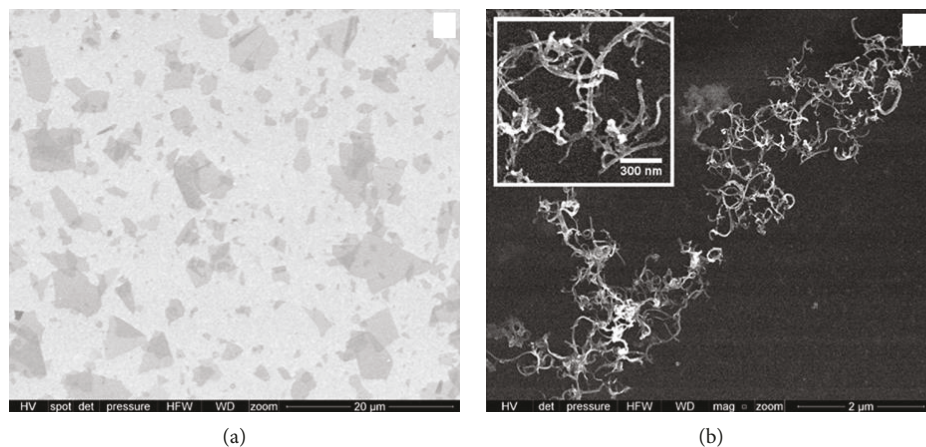


FIGURE 1: SEM images of as-prepared GO sheets (a) and MWCNTs (b).

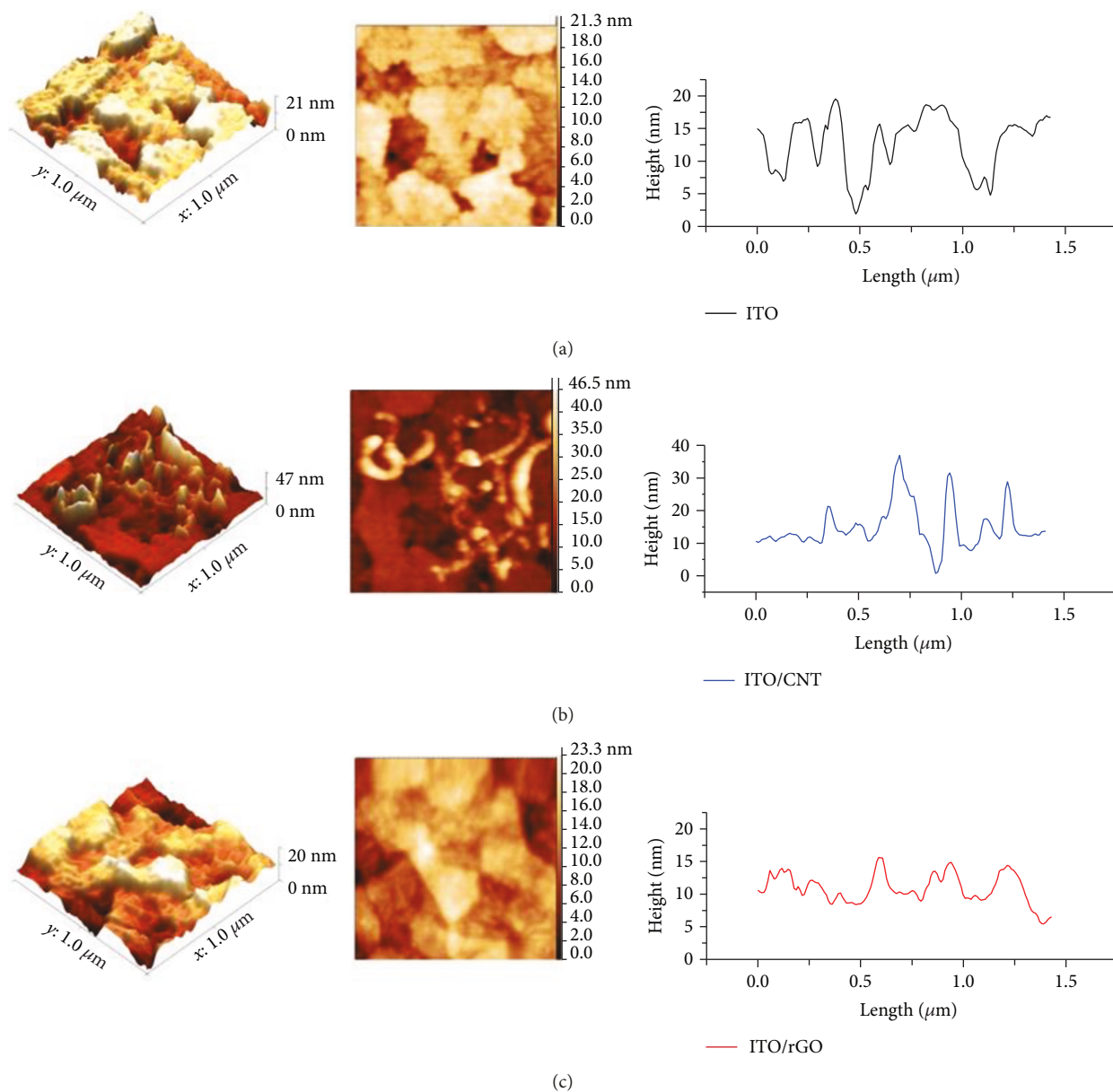


FIGURE 2: AFM images and height profile of (a) ITO, (b) ITO/MWCNT, and (c) ITO/rGO.

TABLE 1: The arithmetic average ( $R_a$ ) and root mean square values ( $R_{ms}$ ) determined from AFM measurements of ITO, ITO/MWCNT, and ITO/rGO samples.

	Surface roughness $R_a$ (nm)	Surface roughness $R_{ms}$ (nm)
ITO	2.82	3.51
ITO/MWCNT	5.33	7.39
ITO/rGO	2.92	3.68

QDs:PCPDTBT with chlorobenzene as a solvent was spin-coated at 1100 rpm for 30 s, followed by an additional drying step at 3000 rpm for 1 min, resulting in an overall active layer thickness of about 80 nm. To form electrical contacts, an aluminum cathode layer of about 80 nm in thickness was deposited by thermal evaporation.

UV-Vis absorption spectra were determined using a TIDAS 100 J&M diode-array spectrometer (Spectralytics, Aalen, Germany). Current density versus voltage ( $J$ - $V$ ) characteristic was measured by a computer-controlled Keithley 2602 source meter measurement system under 100 mW/cm<sup>2</sup> illumination with a solar simulator (LOT-Oriel LSH102) using an AM1.5G filter. CELIV measurements were performed using the all-in-one measurement platform Paios from Fluxim AG.

### 3. Results and Discussion

**3.1. Characterization of Nanocarbon Films.** SEM micrographs of different nanocarbon assemblies deposited onto ITO are shown in Figure 1. It can be observed that the size of the GO sheets (Figure 1(a)) varies from hundreds of nanometer square to 10  $\mu\text{m}^2$ , resulting in an average size of 4.2  $\mu\text{m}^2$ . After mixed-acid oxidation and simultaneous ultrasonication for 24 hours, the original lengths of MWCNTs have been shortened from 1–2  $\mu\text{m}$  to an average length of 356  $\pm$  46 nm.

The optical properties of nanocarbon films have been investigated prior to their utilization in solar cell devices. The transparent nanocarbon thin films of GO and CNT were spin-coated onto ITO glass substrates and then annealed for 1 hour at 300°C under an atmospheric environment. Hence, the GO films produced at this step are considered rGO. The AFM images and morphological profiles of nanocarbon films after annealing are displayed in Figure 2. For comparison, an AFM image of the ITO glass is also featured.

Based on the images in Figure 2 and extracted surface roughness values in Table 1, it is inferred that CNT films possess higher surface roughness as compared to rGO films. Transparency is another important parameter in HTL applications [37]. It is imperative to produce highly transparent nanocarbon films so that an optimal amount of photons can be transmitted towards the photoactive layer. The transparency of different nanocarbon films deposited onto ITO has been measured. The UV-Vis transmission spectra of CNT films and GO films onto the ITO film as well as PEDOT:PSS are illustrated in Figure 3. It is observed that in the range of 600 nm–800 nm, the nanocarbon films deposited

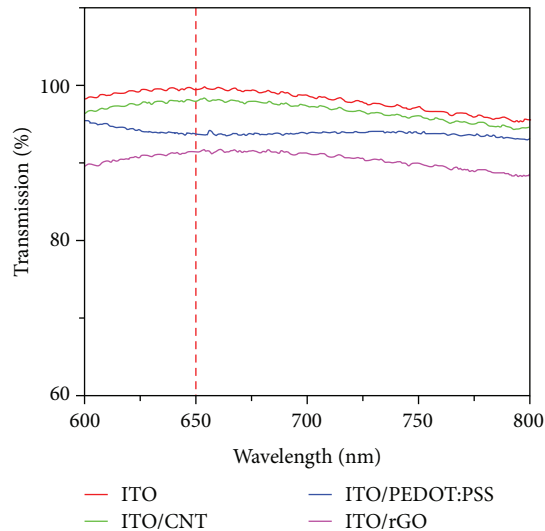


FIGURE 3: Light transmission of the PEDOT:PSS HTL film and nanocarbon films of CNT and rGO, in comparison to an uncoated ITO film.

onto ITO have reasonably high light transparencies as a large portion of the light is transmitted towards the photoactive layer. However, at a wavelength around 650 nm, CNT on ITO shows a reduction in transmission by 2%, while PEDOT:PSS on ITO shows a reduction in light transmission of ca. 5%, and rGO on ITO exhibits the most reduced light transmission by ca. 8%. These results imply that several layers of GO have been deposited onto the ITO glass substrate as it has been reported that every single layer of GO can reduce light transmission of about 2.3% [38].

**3.2. Hybrid Solar Cell Devices with Nanocarbon Films as Buffer and HTL Layers.** All the hybrid solar cell devices were fabricated as described in Materials and Methods. The schematic designs of the different devices are displayed in Figure 4. Typical current-voltage characteristics of the devices are shown in Figure 5. The respective device performance parameters are summarized in Table 2.

Parameters representing resistivity of a material such as shunt/parallel resistance ( $R_{sh}$ ) and series resistance ( $R_s$ ) are useful to further evaluate the device performance, especially in the context of investigating electric contact properties on the interface between the anode and the photoactive layer. The ideal solar cell device should have  $R_s$  values close to zero, while high  $R_{sh}$  is generally preferable. It has been reported that the increasing  $R_s$  is usually concurrent with a decreasing  $R_{sh}$  and vice versa [39–42]. It is known that contact resistance and charge recombination processes are responsible for the increase in  $R_s$  and the decrease in  $R_{sh}$ . The low values of  $R_{sh}$  are leading to leakage of some current and hence to power losses. The high values of  $R_s$  are also responsible for low  $J_{sc}$  values. Many reports have concluded that  $R_s$  plays a dominant role in determining the efficiency of solar cells [43, 44]. Low  $R_s$  values contribute to the increase in electron mobilities in the active layer, ultimately leading to higher PCE values [45].

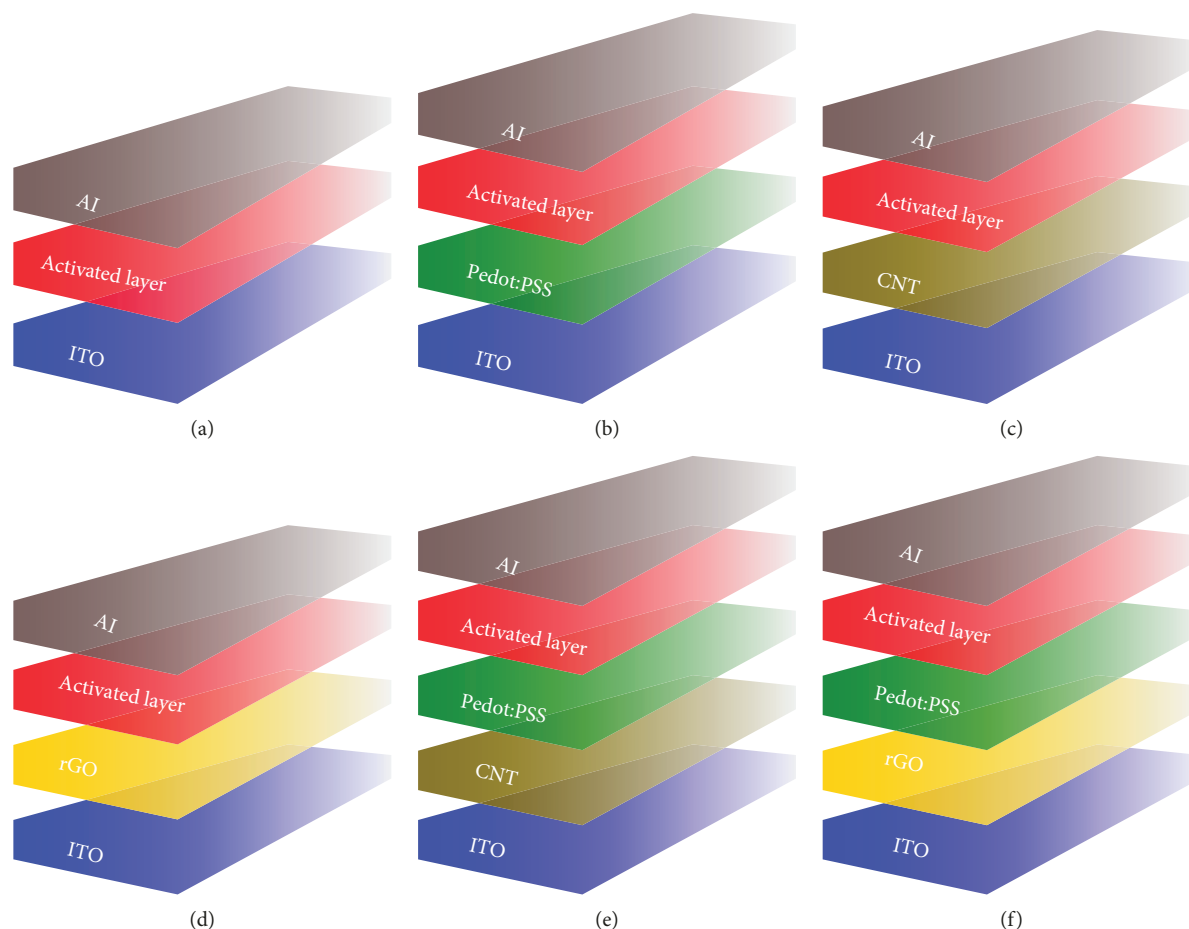


FIGURE 4: Schematic structures of utilized solar cell devices based on different HTL configurations: (a) without any HTL, with HTL of (b) PEDOT:PSS, (c) CNTs, (d) rGO, and with a nanocarbon buffer layer of (e) CNT and (f) rGO between ITO and PEDOT:PSS.

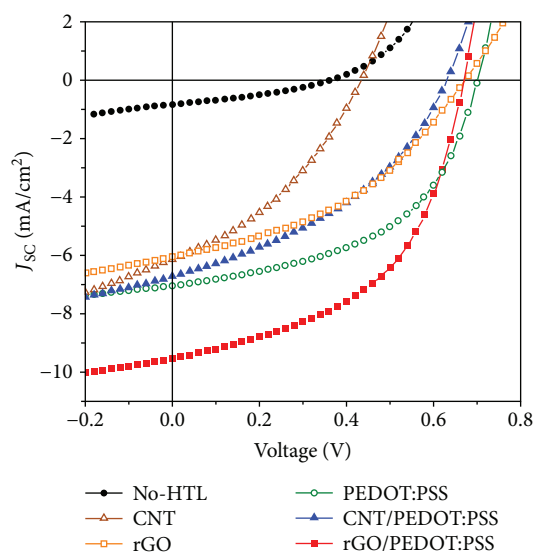


FIGURE 5: Typical  $J$ - $V$  curves of hybrid solar cell devices with different HTL configurations.

The lowest PCE of about 0.1% has been displayed by devices without any HTL (Figure 4(a)), attributable to an interface effect that induces  $R_s$  values of ca.  $126 \Omega\text{cm}^2$  [46].

TABLE 2: Summary of device performance parameters of five types of hybrid solar cells with different HTL configurations.

HTL	$V_{oc}$ (V)	$J_{sc}$ ( $\text{mA}/\text{cm}^2$ )	FF	PCE (%)	$R_{sh}$ ( $\Omega\text{cm}^2$ )	$R_s$ ( $\Omega\text{cm}^2$ )
No-HTL	0.4	0.8	0.4	0.1	413.0	126.0
PEDOT:PSS	0.7	7.0	0.5	2.5	515.5	16.3
CNT	0.4	6.7	0.4	1.0	166.9	27.3
rGO	0.7	6.1	0.4	1.7	403.2	31.3
CNT/PEDOT:PSS	0.6	6.7	0.4	1.7	303.3	26.3
rGO <sup>a</sup> /PEDOT:PSS	0.7	9.5	0.5	3.2	473.9	10.3
rGO <sup>b</sup> /PEDOT:PSS	0.6	6.5	0.6	2.2	448.0	20.0
rGO <sup>c</sup> /PEDOT:PSS	0.7	4.2	0.4	1.2	431.1	41.7

rGO<sup>a</sup>: thermal reduction in air at  $300^\circ\text{C}$  for 1 hour. rGO<sup>b</sup>: thermal reduction in a nitrogen environment at  $300^\circ\text{C}$  for 1 hour. rGO<sup>c</sup>: chemical reduction by thiol functionalization followed by annealing in air at  $300^\circ\text{C}$  for 1 hour.

This high  $R_s$  value results in an extremely low  $J_{sc}$  of  $0.8 \text{ mA}/\text{cm}^2$ . The use of HTL layers out of CNT (Figure 4(c)) and GO (Figure 4(d)) between ITO and the photoactive layer improves the device performance. Compared to the devices without HTL, nanocarbon HTL significantly contributes to lower  $R_s$  values of  $27.3 \Omega\text{cm}^2$  and  $31.3 \Omega\text{cm}^2$  using HTL layers out of CNT and GO, respectively. These results lead

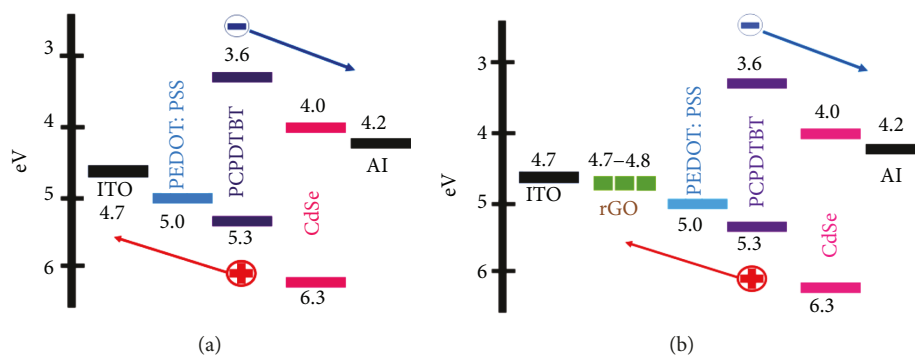


FIGURE 6: Illustration of energy level alignment of devices with (a) PEDOT:PSS as the HTL, (b) PEDOT:PSS HTL, and rGO buffer as a layer. The work function value of thermally reduced GO of about 4.8 eV is taken from Reference [32].

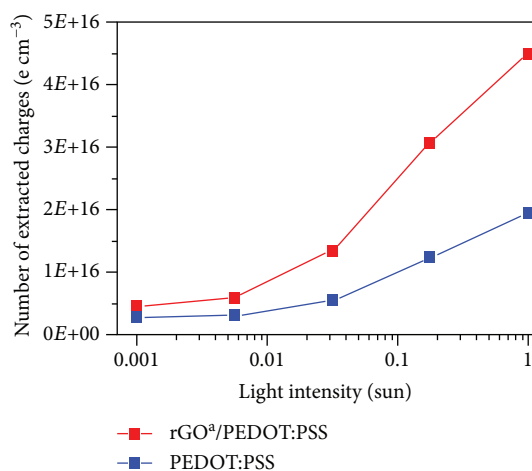


FIGURE 7: The plot of extracted charges vs. light intensity of a hybrid solar cell device based on PEDOT:PSS HTL (reference cells) and cells containing an additional rGO buffer layer.

to a significant improvement in  $J_{SC}$  of up to  $6.7 \text{ mA/cm}^2$  and  $6.1 \text{ mA/cm}^2$  for CNT-based and GO-based devices, respectively. However, PEDOT:PSS as reference HTL (Figure 4(b)) offers lower  $R_s$  values of  $16.3 \Omega \text{ cm}^2$ , which corresponds to a  $J_{SC}$  value of  $7.0 \text{ mA/cm}^2$ . Ultimately, it is evident that a nanocarbon film HTL could enhance PCE from 0.1% (without HTL) to 1.0% and 1.7% for CNT- and rGO-based devices, respectively. In comparison to the performance of rGO-based devices, the relatively low PCE of a CNT-based device is attributed to relatively poor conductivity of the CNTs in question. It has been reported that apart from length shrinkage, the mixed-acid oxidation of MWCNTs also significantly lowers their overall electrical conductivity [47].

Importantly, a remarkable enhancement of PCE was offered by the use of rGO<sup>a</sup>/PEDOT:PSS HTL configuration (Figure 4(f)), revealing a PCE value of 3.2% which is substantially higher than that achieved by PEDOT:PSS-based devices (PCE of 2.5%). This indicates that the thermally reduced rGO buffer layer at an ambient environment was capable of overcoming the energy barrier between ITO and PEDOT:PSS, resulting in an improved hole extraction as illustrated in Figure 6.

Figure 6 illustrates the energy level of solar cells with PEDOT:PSS as the HTL and rGO buffer layer. Based on the literature, WF values of ITO and PEDOT:PSS are 4.7 eV [48–50] and 5.0 eV [51], respectively. HOMO and LUMO levels of PCPDTBT are -5.3 eV and -3.5 eV, respectively, and were adapted from Reference [52]. It has been reported that 6 nm CdSe QDs have valence and conduction band edges of about -5.59 eV and -3.62 eV, respectively [53]. The simplest method of GO reduction is achieved by thermal annealing in the air (a). However, it has been found that the oxygen content at the GO surface cannot be easily removed, even at an elevated temperature up to  $1100^\circ\text{C}$  and ultrahigh vacuum [54]. It has been reported that annealing of GO at  $350^\circ\text{C}$  caused a WF decrease by 0.3 eV [32]. Starting from a pristine GO with a reported WF of about 5.0–5.1 eV [55, 56], the WF is lowered after annealing to 4.7–4.8 eV [32].

**3.3. CELIV Measurements.** In order to understand the role of the thermally reduced GO buffer layer in enhancing the performance of solar cell devices, CELIV (charge extraction by linearly increasing voltage) measurements have been performed at Fluxim AG [57]. The reference device, which is based solely on PEDOT:PSS as the HTL, is compared to a device with an additional thermally reduced GO buffer layer. The plots of extracted charges versus light intensity from CELIV measurements are depicted in Figure 7. In Table 3, the extracted charges in the dark and under illumination are summarized additionally.

It is observable in Figure 7 that the amount of extracted charges increases along with the increase in light intensity. Interestingly, the increase in extracted charges in the device with a rGO<sup>a</sup> buffer layer is more striking as compared to that in the reference cell. This result is confirmed by the ratio of charges extracted due to illumination (QL-QD) to charges extracted in the dark (QD) for the device with a rGO<sup>a</sup> buffer layer of about 8.72, while PEDOT:PSS-based devices display only a ratio of 5.92 (Table 3). It indicates that the charge extraction in polymer/CdSe QD solar cell devices is more efficient when an additional rGO buffer layer is inserted between PEDOT:PSS and the photoactive layer.

**3.4. Influence of the GO Buffer Layer Reduction Degree on the Solar Cell Device Performance.** As the enhanced performance was exhibited, the effect of GO reduction on the performance

TABLE 3: Summary of extracted charges in the dark (QD) and under illumination (QL), calculated amount of additionally extracted charges due to illumination (QL-QD), and the ratio of these charges to charges extracted in the dark (QL-QD)/QD of a solar cell device with PEDOT:PSS as the HTL and a device with an additional rGO as the buffer layer.

	Extracted charges in the dark (QD) ( $e\text{ cm}^{-3}$ )	Extracted charges under illumination (QL) ( $e\text{ cm}^{-3}$ )	(QL-QD) ( $e\text{ cm}^{-3}$ )	(QL-QD)/QD
PEDOT:PSS	$2.81E + 15$	$1.94E + 16$	$1.66E + 16$	5.92
rGO <sup>a</sup> /PEDOT:PSS	$4.62E + 15$	$4.48E + 16$	$4.02E + 16$	8.72

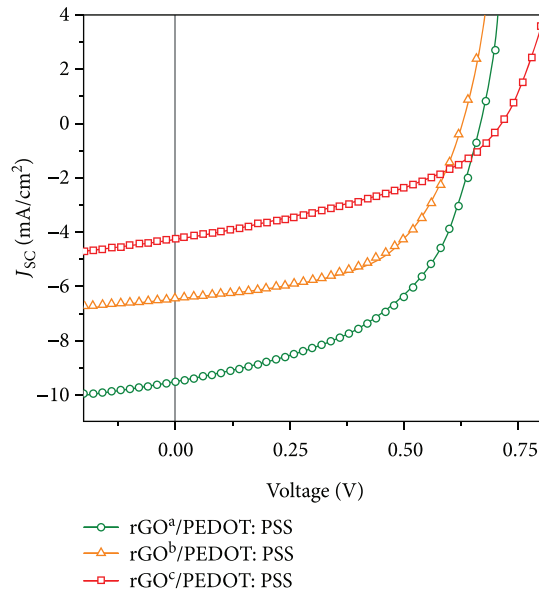


FIGURE 8:  $J$ - $V$  curves of typical hybrid solar cell devices based on three different reduction conditions for the rGO buffer layer: (a) rGO<sup>a</sup>: thermal reduction in air, (b) rGO<sup>b</sup>: thermal reduction in a nitrogen atmosphere, and (c) rGO<sup>c</sup>: a combination of chemical and thermal reduction.

of hybrid solar cell devices was further scrutinized. Two other procedures of GO reduction are utilized, resulting in the three different degrees of GO reduction. The first is weak reduction (a), accomplished by thermal reduction in air at 300°C for 1 hour. The second is medium reduction (b), referring to thermal annealing in a nitrogen environment at 300°C for 1 hour. The third one is strong reduction (c), obtained by a combination of chemical and thermal reductions, in which GO is chemically reduced via thiol functionalization followed by thermal annealing under air atmosphere at 300°C for 1 hour. The  $J$ - $V$  curves of the devices based on the three different reductive degrees are shown in Figure 8.

Figure 8 clearly shows the effect of the rGO reduction degree on the device performance of hybrid solar cells. Apparently, the PCEs of the solar cell devices decrease following the reduction degree of the GO buffer layer. The weakly reduced GO, which is obtained by annealing in air at 300°C, exhibited the best device performance as compared to its two counterparts with a higher reduction degree. This approach results in  $J_{SC}$  of as high as 9.52 mA/cm<sup>2</sup>, corresponding to PCE of ca. 3.21%, which is the highest value in this work. Medium reduction of GO, which is achieved by annealing inside a nitrogen-filled glove box, leads to the rGO buffer layer with a lower  $J_{SC}$  and PCE of

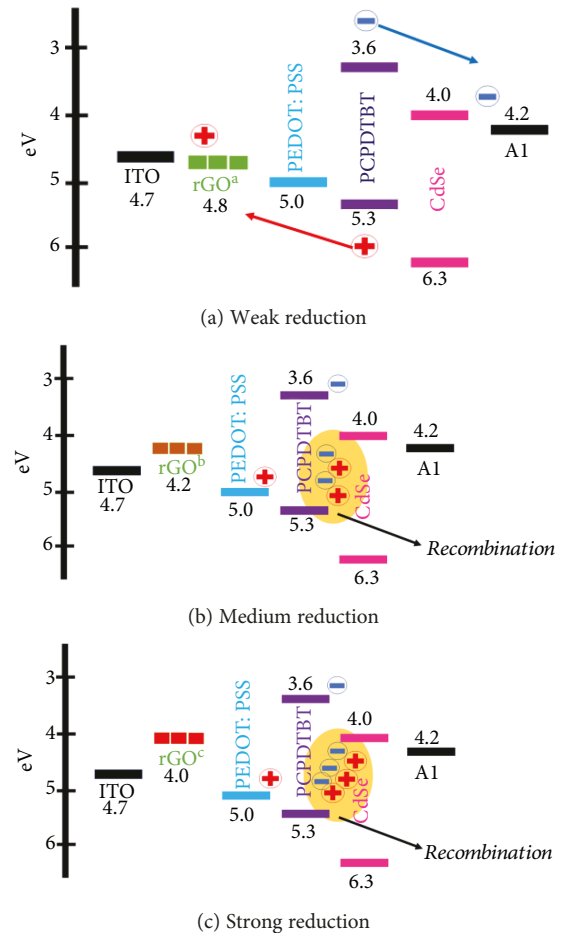


FIGURE 9: Illustration of the energy level of utilized solar cell devices based on the three different reduction degrees of rGO buffer layers. Lower WF of medium (b) and strong (c) reduction is resulting in a mismatch of the energy levels leading to a barrier for hole transport and hole extraction. As a consequence, more recombination processes at the interface are occurring.

about 6.47 mA/cm<sup>2</sup> and 2.19%, respectively. The performance is observed in strongly reduced GO, by thermal annealing of chemically thiolated rGO, and is leading to a device with  $J_{SC}$  of 4.26 mA/cm<sup>2</sup> and a PCE of 1.19%.

We suggest that the aforementioned phenomena are the results of WF dependence on the degree of reduction. The WF from annealing under air atmosphere (weak reduction) is relatively different from that obtained in a nitrogen-filled glove box (medium reduction). The reduction in a nitrogen-rich environment of a glovebox is comparable to that in NH<sub>3</sub> [58] and the hydrazine method [54]. By these methods,

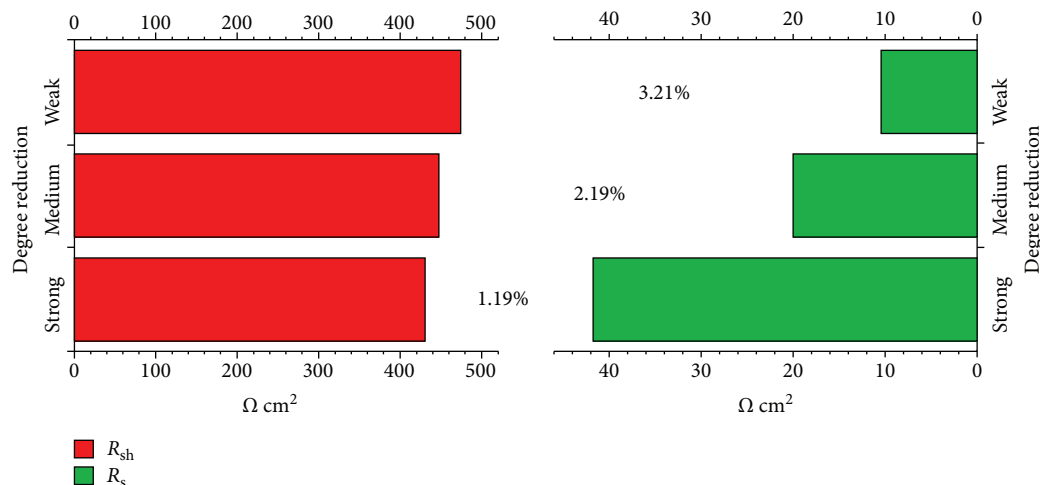


FIGURE 10: Influence of the reduction degree of rGO buffer layers on  $R_s$  and  $R_{sh}$  of respective devices.

N-doped graphene with WF of ca. 4.2 eV was obtained [59–62]. Therefore, strong reduction is obtained under condition (c), and it is expected to bring about a much lower WF. It has been reported that thiol (-SH) groups inserted in GO would lower the WF down to 4.0 eV [63]. The illustration of energy level diagrams of hybrid solar cell devices based on rGO buffer layers with different degrees of reduction is depicted in Figure 9. Their WF values have been adopted from literature.

One can infer from Figure 9 that the WF of a weakly reduced GO (rGO<sup>a</sup>) is preferred as a buffer layer, while both moderate reduction (rGO<sup>b</sup>) and strong reduction (rGO<sup>c</sup>) of GO produce layers with lower WFs, resulting in a mismatch of energy level which limits hole transport and hole extraction to the anode. In these cases, charges are accumulating at the donor-acceptor interface, leading to increased bimolecular charge recombination. Ultimately, charge recombination produces low current density and PCE values.

Figure 10 further illustrates another consequence of the mismatch of band level alignment. With increasing degree of reduction of rGO,  $R_s$  becomes substantially higher, while  $R_{sh}$  slightly decreases. It has been reported that higher  $R_s$  values constitute poor charge transport, promoting charge recombination processes [64]. Ultimately, this charge recombination as a result of low WF of rGO would lower  $J_{SC}$  and, in turn, the overall PCE values for hybrid solar cell devices as shown in Table 1.

#### 4. Conclusions

In summary, the PCE enhancement of hybrid BHJ solar cells by ca. 30% has been facilitated using rGO as an additional buffer layer. This layer is inserted in between the ITO anode and the PEDOT:PSS layer. The enhancement was achieved as a result of an optimized energy level alignment, leading to a better hole extraction which was confirmed by CELIV measurements. This is accompanied by a significant decrease in  $R_s$  and an increase in  $J_{SC}$ . It is also shown that the degree to which GO is reduced strongly affects the performance of solar cell devices. Devices with thermally reduced rGO buffer

layers exhibited the highest PCE value of up to 3.2%, while reference cells employing solely PEDOT:PSS as the HTL reached PCE values of only 2.5%. The superior performance of devices with an additional rGO buffer layer can be attributed to the betterment of charge extraction towards the anode. The PCE of devices based on solely rGO films as HTLs is only 30% lower than that of a PEDOT:PSS-based reference device. Further tuning of the work function is possible and might lead to further device improvements. This work demonstrates the excellent potential of solution-processed rGO as an alternative HTL material in hybrid BHJ solar cells. It should also be noted that our findings in this work might also pave the way for applications in various solar cell types as well as other optoelectronic applications.

#### Data Availability

The data used to support the findings of this study are included within the article.

#### Conflicts of Interest

The authors declare that they have no conflicts of interest regarding the publication of this paper.

#### Acknowledgments

This research publication is supported by the United States Agency for International Development (USAID) through the Sustainable Higher Education Research Alliance (SHERA) Program for Universitas Indonesia's Scientific Modeling, Application, Research, and Training for City-centered Innovation and Technology (SMART CITY) Project (Grant #AID-497-A-1600004, Sub-Grant #IIE-00000078-UI-1).

#### References

- [1] Y. Zhou, M. Eck, and M. Kruger, "Bulk-heterojunction hybrid solar cells based on colloidal nanocrystals and conjugated polymers," *Energy & Environmental Science*, vol. 3, no. 12, pp. 1851–1864, 2010.

- [2] M. Wright and A. Uddin, "Organic—inorganic hybrid solar cells: a comparative review," *Solar Energy Materials and Solar Cells*, vol. 107, pp. 87–111, 2012.
- [3] R. Zhou, R. Stalder, D. Xie et al., "Enhancing the efficiency of solution-processed polymer:colloidal nanocrystal hybrid photovoltaic cells using ethanedithiol treatment," *ACS Nano*, vol. 7, no. 6, pp. 4846–4854, 2013.
- [4] G. Dennler, M. C. Scharber, and C. J. Brabec, "Polymer-fullerene bulk-heterojunction solar cells," *Advanced Materials*, vol. 21, no. 13, pp. 1323–1338, 2009.
- [5] J. Y. Kim, K. Lee, N. E. Coates et al., "Efficient tandem polymer solar cells fabricated by all-solution processing," *Science*, vol. 317, no. 5835, pp. 222–225, 2007.
- [6] C. Jonda, A. B. R. Mayer, U. Stolz, A. Elschner, and A. Karbach, "Surface roughness effects and their influence on the degradation of organic light emitting devices," *Journal of Materials Science*, vol. 35, no. 22, pp. 5645–5651, 2000.
- [7] M. Jørgensen, K. Norrman, and F. C. Krebs, "Stability/degradation of polymer solar cells," *Solar Energy Materials and Solar Cells*, vol. 92, no. 7, pp. 686–714, 2008.
- [8] C.-H. M. Chuang, P. R. Brown, V. Bulović, and M. G. Bawendi, "Improved performance and stability in quantum dot solar cells through band alignment engineering," *Nature Materials*, vol. 13, no. 8, pp. 796–801, 2014.
- [9] M. P. de Jong, L. J. van IJzendoorn, and M. J. A. de Voigt, "Stability of the interface between indium-tin-oxide and poly(3,4-ethylenedioxythiophene)/poly(styrenesulfonate) in polymer light-emitting diodes," *Applied Physics Letters*, vol. 77, no. 14, pp. 2255–2257, 2000.
- [10] K. W. Wong, H. L. Yip, Y. Luo et al., "Blocking reactions between indium-tin oxide and poly(3,4-ethylene dioxythiophene):poly(styrene sulphonate) with a self-assembly monolayer," *Applied Physics Letters*, vol. 80, no. 15, pp. 2788–2790, 2002.
- [11] Y.-H. Kim, S.-H. Lee, J. Noh, and S.-H. Han, "Performance and stability of electroluminescent device with self-assembled layers of poly(3,4-ethylenedioxythiophene)-poly(styrenesulfonate) and polyelectrolytes," *Thin Solid Films*, vol. 510, no. 1-2, pp. 305–310, 2006.
- [12] C. Guillén and J. Herrero, "High-performance electrodes for organic photovoltaics," in *Organic Photovoltaics*, pp. 399–423, Wiley-VCH Verlag GmbH & Co. KGaA, 2009.
- [13] S. Züfle, M. T. Neukom, S. Altazin et al., "An effective area approach to model lateral degradation in organic solar cells," *Advanced Energy Materials*, vol. 5, no. 20, article 1500835, 2015.
- [14] L.-C. Huang, H.-W. Liu, C.-W. Liang, T.-R. Chou, L. Wang, and C.-Y. Chao, "Self-assembled multilayers of modified ITO in polymer solar cells by soft-imprinting," *Soft Matter*, vol. 8, no. 5, pp. 1467–1472, 2012.
- [15] K. Norrman, M. V. Madsen, S. A. Gevorgyan, and F. C. Krebs, "Degradation patterns in water and oxygen of an inverted polymer solar cell," *Journal of the American Chemical Society*, vol. 132, no. 47, pp. 16883–16892, 2010.
- [16] I. Winter, C. Reese, J. Holmes, G. Heywang, and F. Jonas, "The thermal ageing of poly(3,4-ethylenedioxythiophene). An investigation by X-ray absorption and X-ray photoelectron spectroscopy," *Chemical Physics*, vol. 194, no. 1, pp. 207–213, 1995.
- [17] Y. Gao, H.-L. Yip, S. K. Hau et al., "Anode modification of inverted polymer solar cells using graphene oxide," *Applied Physics Letters*, vol. 97, no. 20, article 203306, 2010.
- [18] D. W. Chang, H.-J. Choi, A. Filer, and J.-B. Baek, "Graphene in photovoltaic applications: organic photovoltaic cells (OPVs) and dye-sensitized solar cells (DSSCs)," *Journal of Materials Chemistry A*, vol. 2, no. 31, pp. 12136–12149, 2014.
- [19] X. Wang, L. Zhi, and K. Müllen, "Transparent, conductive graphene electrodes for dye-sensitized solar cells," *Nano Letters*, vol. 8, no. 1, pp. 323–327, 2008.
- [20] G. Eda, G. Fanchini, and M. Chhowalla, "Large-area ultrathin films of reduced graphene oxide as a transparent and flexible electronic material," *Nature Nanotechnology*, vol. 3, no. 5, pp. 270–274, 2008.
- [21] A. Al-Hamry, H. Kang, E. Sowade et al., "Tuning the reduction and conductivity of solution-processed graphene oxide by intense pulsed light," *Carbon*, vol. 102, pp. 236–244, 2016.
- [22] R. Garg, N. K. Dutta, and N. R. Choudhury, "Work function engineering of graphene," *Nanomaterials*, vol. 4, no. 2, pp. 267–300, 2014.
- [23] D. R. Dreyer, S. Park, C. W. Bielawski, and R. S. Ruoff, "The chemistry of graphene oxide," *Chemical Society Reviews*, vol. 39, no. 1, pp. 228–240, 2010.
- [24] C. Mattevi, G. Eda, S. Agnoli et al., "Evolution of electrical, chemical, and structural properties of transparent and conducting chemically derived graphene thin films," *Advanced Functional Materials*, vol. 19, no. 16, pp. 2577–2583, 2009.
- [25] J. Liu, M. Durstock, and L. Dai, "Graphene oxide derivatives as hole- and electron-extraction layers for high-performance polymer solar cells," *Energy & Environmental Science*, vol. 7, no. 4, pp. 1297–1306, 2014.
- [26] S. Mao, H. Pu, and J. Chen, "Graphene oxide and its reduction: modeling and experimental progress," *RSC Advances*, vol. 2, no. 7, pp. 2643–2662, 2012.
- [27] D. C. Marcano, D. V. Kosynkin, J. M. Berlin et al., "Improved synthesis of graphene oxide," *ACS Nano*, vol. 4, no. 8, pp. 4806–4814, 2010.
- [28] J. Chen, B. Yao, C. Li, and G. Shi, "An improved Hummers method for eco-friendly synthesis of graphene oxide," *Carbon*, vol. 64, pp. 225–229, 2013.
- [29] W. S. Hummers Jr and R. E. Offeman, "Preparation of graphitic oxide," *Journal of the American Chemical Society*, vol. 80, no. 6, p. 1339, 1958.
- [30] P. V. Kumar, M. Bernardi, and J. C. Grossman, "The impact of functionalization on the stability, work function, and photoluminescence of reduced graphene oxide," *ACS Nano*, vol. 7, no. 2, pp. 1638–1645, 2013.
- [31] M. Mishra, R. K. Joshi, S. Ojha, D. Kanjilal, and T. Mohanty, "Role of oxygen in the work function modification at various stages of chemically synthesized graphene," *Journal of Physical Chemistry C*, vol. 117, no. 38, pp. 19746–19750, 2013.
- [32] L. Sygellou, G. Paterakis, C. Galiotis, and D. Tasis, "Work function tuning of reduced graphene oxide thin films," *Journal of Physical Chemistry C*, vol. 120, no. 1, pp. 281–290, 2016.
- [33] X. Peng, F. Tang, and A. Copple, "Engineering the work function of armchair graphene nanoribbons using strain and functional species: a first principles study," *Journal of Physics: Condensed Matter*, vol. 24, no. 7, article 075501, 2012.
- [34] C. V. Pham, M. Eck, and M. Krueger, "Thiol functionalized reduced graphene oxide as a base material for novel graphene-nanoparticle hybrid composites," *Chemical Engineering Journal*, vol. 231, pp. 146–154, 2013.

- [35] Y. Yuan, F.-S. Riehle, H. Gu, R. Thomann, G. Urban, and M. Krüger, "Critical parameters for the scale-up synthesis of quantum dots," *Journal of Nanoscience and Nanotechnology*, vol. 10, no. 9, pp. 6041–6045, 2010.
- [36] Y. Zhou, F. S. Riehle, Y. Yuan et al., "Improved efficiency of hybrid solar cells based on non-ligand-exchanged CdSe quantum dots and poly(3-hexylthiophene)," *Applied Physics Letters*, vol. 96, no. 1, pp. 133041–133044, 2010.
- [37] J. Liu, Y. Xue, and L. Dai, "Sulfated graphene oxide as a hole-extraction layer in high-performance polymer solar cells," *Journal of Physical Chemistry Letters*, vol. 3, no. 14, pp. 1928–1933, 2012.
- [38] R. R. Nair, P. Blake, A. N. Grigorenko et al., "Fine structure constant defines visual transparency of graphene," *Science*, vol. 320, no. 5881, p. 1308, 2008.
- [39] T. L. Chen, J. J.-A. Chen, L. Catane, and B. Ma, "Fully solution processed p-i-n organic solar cells with an industrial pigment – quinacridone," *Organic Electronics*, vol. 12, no. 7, pp. 1126–1131, 2011.
- [40] K. Wang, Y. Zheng, G. Xu, and X. Xu, "The inverse correlation between series resistance and parallel resistance of small molecule organic solar cells," *Progress in Natural Science*, vol. 25, no. 4, pp. 323–326, 2015.
- [41] M. Rusu, S. Wiesner, I. Lauermaun et al., "Formation of charge-selective Mg–Ag electrodes to CuPc:C60 blend layers," *Applied Physics Letters*, vol. 97, no. 7, article 073504, 2010.
- [42] M. T. Lloyd, A. C. Mayer, A. S. Tayi et al., "Photovoltaic cells from a soluble pentacene derivative," *Organic Electronics*, vol. 7, no. 5, pp. 243–248, 2006.
- [43] S. M. Sze and K. K. Ng, "p-n junctions," in *Physics of Semiconductor Devices*, pp. 77–133, John Wiley & Sons, Inc, 2006.
- [44] J. Xue, S. Uchida, B. P. Rand, and S. R. Forrest, "4.2% efficient organic photovoltaic cells with low series resistances," *Applied Physics Letters*, vol. 84, no. 16, pp. 3013–3015, 2004.
- [45] J. D. Servaites, S. Yeganeh, T. J. Marks, and M. A. Ratner, "Efficiency enhancement in organic photovoltaic cells: consequences of optimizing series resistance," *Advanced Functional Materials*, vol. 20, no. 1, pp. 97–104, 2010.
- [46] W. Tress, "Interplay between electrodes and active materials: the open-circuit voltage and S-shaped J-V curves," in *Organic Solar Cells: Theory, Experiment, and Device Simulation*, pp. 315–357, Springer International Publishing, Cham, 2014.
- [47] C. H. Lau, R. Cervini, S. R. Clarke et al., "The effect of functionalization on structure and electrical conductivity of multi-walled carbon nanotubes," *Journal of Nanoparticle Research*, vol. 10, Supplement 1, pp. 77–88, 2008.
- [48] N. Balasubramanian and A. Subrahmanyam, "Studies on evaporated indium tin oxide (ITO)/silicon junctions and an estimation of ITO work function," *Journal of the Electrochemical Society*, vol. 138, no. 1, pp. 322–324, 1991.
- [49] I. D. Parker, "Carrier tunneling and device characteristics in polymer light-emitting diodes," *Journal of Applied Physics*, vol. 75, no. 3, pp. 1656–1666, 1994.
- [50] Y. Park, V. Choong, Y. Gao, B. R. Hsieh, and C. W. Tang, "Work function of indium tin oxide transparent conductor measured by photoelectron spectroscopy," *Applied Physics Letters*, vol. 68, no. 19, pp. 2699–2701, 1996.
- [51] M. C. Scharber, D. Mühlbacher, M. Koppe et al., "Design rules for donors in bulk-heterojunction solar cells—towards 10 % energy-conversion efficiency," *Advanced Materials*, vol. 18, no. 6, pp. 789–794, 2006.
- [52] D. Mühlbacher, M. Scharber, M. Morana et al., "High photovoltaic performance of a low-bandgap polymer," *Advanced Materials*, vol. 18, no. 21, pp. 2884–2889, 2006.
- [53] C. Querner, P. Reiss, S. Sadki, M. Zagorska, and A. Pron, "Size and ligand effects on the electrochemical and spectroelectrochemical responses of CdSe nanocrystals," *Physical Chemistry Chemical Physics*, vol. 7, no. 17, pp. 3204–3209, 2005.
- [54] D. Yang, A. Velamakanni, G. Bozoklu et al., "Chemical analysis of graphene oxide films after heat and chemical treatments by X-ray photoelectron and micro-Raman spectroscopy," *Carbon*, vol. 47, no. 1, pp. 145–152, 2009.
- [55] D. Yang, L. Zhou, L. Chen, B. Zhao, J. Zhang, and C. Li, "Chemically modified graphene oxides as a hole transport layer in organic solar cells," *Chemical Communications*, vol. 48, no. 65, pp. 8078–8080, 2012.
- [56] R. Wu, Y. Wang, L. Chen, L. Huang, and Y. Chen, "Control of the oxidation level of graphene oxide for high efficiency polymer solar cells," *RSC Advances*, vol. 5, no. 61, pp. 49182–49187, 2015.
- [57] M. T. Neukom, S. Züfle, and B. Ruhstaller, "Reliable extraction of organic solar cell parameters by combining steady-state and transient techniques," *Organic Electronics*, vol. 13, no. 12, pp. 2910–2916, 2012.
- [58] X. Li, H. Wang, J. T. Robinson, H. Sanchez, G. Diankov, and H. Dai, "Simultaneous nitrogen doping and reduction of graphene oxide," *Journal of the American Chemical Society*, vol. 131, no. 43, pp. 15939–15944, 2009.
- [59] C. K. Chua and M. Pumera, "Chemical reduction of graphene oxide: a synthetic chemistry viewpoint," *Chemical Society Reviews*, vol. 43, no. 1, pp. 291–312, 2014.
- [60] D. Du, P. Li, and J. Ouyang, "Nitrogen-doped reduced graphene oxide prepared by simultaneous thermal reduction and nitrogen doping of graphene oxide in air and its application as an electrocatalyst," *ACS Applied Materials & Interfaces*, vol. 7, no. 48, pp. 26952–26958, 2015.
- [61] T. Kuila, A. K. Mishra, P. Khanra, N. H. Kim, and J. H. Lee, "Recent advances in the efficient reduction of graphene oxide and its application as energy storage electrode materials," *Nanoscale*, vol. 5, no. 1, pp. 52–71, 2013.
- [62] Y. Wang, Y. Shao, D. W. Matson, J. Li, and Y. Lin, "Nitrogen-doped graphene and its application in electrochemical biosensing," *ACS Nano*, vol. 4, no. 4, pp. 1790–1798, 2010.
- [63] Z. Hu, C. Li, R. Nie, Y.-Q. Li, J.-X. Tang, and X. Deng, "Biomaterial functionalized graphene oxides with tunable work function for high sensitive organic photodetectors," *RSC Advances*, vol. 5, no. 120, pp. 99431–99438, 2015.
- [64] R. A. Street, M. Schoendorf, A. Roy, and J. H. Lee, "Interface state recombination in organic solar cells," *Physical Review B*, vol. 81, no. 20, article 205307, 2010.



**Hindawi**  
Submit your manuscripts at  
[www.hindawi.com](http://www.hindawi.com)

